

ARTICLE

Role of the tensile constitutive modeling on the structural response of fiber reinforced concrete flat slabs: A numerical study

Giulio Zani  | Paolo Martinelli  | Marco di Prisco 

Department of Civil and Environmental Engineering, Politecnico di Milano, Milan, Italy

Correspondence

Paolo Martinelli, Department of Civil and Environmental Engineering, Politecnico di Milano, Milan, Italy.

Email: paolo.martinelli@polimi.it

Abstract

For decades, fiber reinforced concrete (FRC) has been primarily used in elements for which the consequences of potential failure are minor, like slabs on grade and precast tunnel segments, just to name a few examples. With reference to slabs supported on walls and/or columns, the use of fibers as partial or main reinforcement has increased over the last 15 years. Despite the existence of advanced design codes like the *fib* Model Code 2010, experimental data, and standing buildings that prove the technical feasibility of FRC, there are still barriers for its use at a wider scale. Technical aspects such as the uncertainties in the identification procedure of FRC uniaxial tensile laws and the influence of the FRC post-cracking strength class on the serviceability and ultimate limit states response are among the factors that prevent a larger diffusion of FRC. In this paper, the role played by several tensile post-cracking constitutive models—among those most commonly used both in research and in design practice—on the structural response of FRC flat slabs is investigated. The effect of numerical modeling choices such as (i) the influence of shell or brick elements and (ii) the influence of material homogeneity or heterogeneity along the slab thickness on the structural response of FRC flat slabs is also examined.

KEYWORDS

fiber reinforced concrete, flat slabs, numerical modeling, uniaxial tensile behavior

1 | INTRODUCTION

Fiber reinforced concrete (FRC) is a composite construction material made of a cement-based matrix that

incorporates randomly dispersed fibers. The inclusion of fibers in the matrix allows the enhancement of the post-cracking tensile strength, with an increase of the fracture energy positively affecting the structural response at both the serviceability (SLS) and ultimate (ULS) limit states.¹

For decades, FRC has been primarily used in elements for which the consequences of potential failure are minor, like slabs on grade,^{2–4} precast tunnel segments,^{5–7} reinforced earth-retaining walls,⁸ and sewerage pipes.⁹

Discussion on this paper must be submitted within two months of the print publication. The discussion will then be published in print, along with the authors' closure, if any, approximately nine months after the print publication.

This is an open access article under the terms of the [Creative Commons Attribution-NonCommercial-NoDerivs](https://creativecommons.org/licenses/by-nc-nd/4.0/) License, which permits use and distribution in any medium, provided the original work is properly cited, the use is non-commercial and no modifications or adaptations are made.

© 2022 The Authors. *Structural Concrete* published by John Wiley & Sons Ltd on behalf of International Federation for Structural Concrete.

Moreover, all these structural elements are subjected to relatively low bending moments—usually below the cracking limit—during transient and service loading situations and the stress redistribution at failure is always guaranteed by soil interaction.

The publication of advanced design codes as the *fib* Model Code 2010¹⁰ has fostered the use of FRC in the construction industry, thanks to the introduction of unified classification rules—based on the concept of FRC post-cracking (or residual) strength classes—and to simplified constitutive behaviors. As consequence, in recent years the diffusion of FRC into common design practice has continuously increased.

With reference to elevated slabs supported on walls and/or columns (this last referred also as flat slabs), the use of fibers (especially steel fibers) as partial or main reinforcement has increased over the last 15 years. Successful examples of steel fiber reinforced concrete (SFRC) flat slabs usually combine traditional steel high-bond bars with steel fibers.¹¹ Steel bars are employed in critical regions to activate ductile failure mechanisms at the onset of collapse and to prevent progressive failure in accidental load scenarios. A good design philosophy can employ fibers for the “average” values of bending moment acting on the slab, while the peak stresses and the robustness are entrusted to ordinary steel bars in the areas where higher bending moments are expected and along the chains connecting the supports. The benefits of the addition of fibers in reinforced concrete (RC) slabs at SLS consist in a reduction of the crack opening, with a consequent lowering of the stress levels in the steel bars at the crack location. At ULS, the use of fibers allows increasing the ultimate bending and shear capacities. It is worth noting that, in those sections devoid of reinforcing bars, the whole bending capacity of the slab relies only on fiber contribution.

The literature reports several experimental studies on the use of FRC in flat slabs (see, e.g., the work of Hedebratt and Silfverbrand,¹² Salehian and Barros,¹³ and di Prisco et al.,¹⁴ among the others). A comprehensive state-of-art on FRC slabs is given by Nogales and de la Fuente.¹⁵ Eighteen studies were analyzed by the authors, and most of them focused on the use of SFRC and on the comparison between hybrid reinforced concrete (rebar + fibers) and traditional RC elements.

Some examples of SFRC technology applied in real projects for the construction of residential flat slabs are reported in the literature: a two-storey family house (Italy), an industrial building in Como (Italy), the Ditton Nams shopping mall (Latvia), the Triangle office building (Estonia), the Rocca Al-Mare office tower (Estonia), and the LKS office building (Spain). A detailed description of the first two examples can be found in Martinelli et al.¹¹ and di Prisco et al.,¹⁶ while a brief description of the last three examples can be found in Aidarov et al.¹⁷

Despite the existence of advanced design codes like the *fib* Model Code 2010,¹⁰ guidelines specifically oriented to FRC flat slabs,¹⁸ and experimental data and real buildings that prove the technical feasibility of FRC, there are still barriers for its use at a wider scale. Technical aspects such as the uncertainties in the identification procedure of the FRC uniaxial tensile law and the influence of the FRC post-cracking strength class on the SLS and ULS response require further research.

Available guidelines and Standards such as the ACI 544,¹⁹ RILEM TC162-TDF,²⁰ CNR-DT 204,²¹ and the *fib* Model Code 2010¹⁰ provide simplified tensile laws mainly conceived for sectional calculations based on a plane-section kinematic model. Their use in the context of non-linear modeling has shown a good ability to predict the ultimate behavior of beam elements, but limitations in capturing serviceability responses, hence introducing additional uncertainties in the simulation of statically indeterminate elements and evolution of cracking patterns. Among the mentioned guidelines and Standards, the *fib* Model Code 2010¹⁰ is considered by practitioners and researchers as one of the most advanced documents, and is being referenced in the new generation of the Eurocode 2 and in the *fib* Model Code 2020.

In the literature, improvements in the simulation effectiveness based on full inverse approaches or adjustments of sectional equilibrium equations at reference crack openings are documented.^{22–24} The aim of this work is to clarify, starting from the *fib* Model Code 2010¹⁰ proposal, the role of the adoption of different tensile post-cracking laws—mostly entailing alterations in the crack opening range 0–0.05 mm—on the prediction of the structural response of FRC flat slabs. The formulations are based on well-known procedures combining the plain concrete behavior (*fib* Model Code 1990²⁵; *fib* Model Code 2010¹⁰) with the fiber pull-out response (*fib* Model Code 2010¹⁰; di Prisco et al.²³), avoiding the use of time-consuming inverse analyses targeting notched beam results. A numerical finite element (FE) approach accounting for material nonlinearities is followed to pursue the objective. The reliability of the numerical results is assessed by comparison with experimental data available in the literature. Given the purpose of the work, it was decided to analyze a full-scale FRC flat slab prototype without ordinary reinforcing bars. Numerical issues in modeling FRC flat slabs are also discussed.

2 | DESCRIPTION OF THE FLAT SLAB CASE STUDY

An SFRC flat slab without traditional reinforcement was built and tested at the Belgian Building Research

Institute (BBRI), in Limelette, Belgium.²⁶ The slab consisted of 3×3 -bays (panels) supported by 16 circular concrete columns with a concrete class C30/37 and a diameter of 0.3 m (Figure 1). The slab had a nominal thickness of 0.2 m. The center distance between the columns was 6 m along both the orthogonal directions, while the slab full-size was 18.3×18.3 m². The columns were reinforced with six longitudinal steel bars of diameter 12 mm, interconnected with circular stirrups. The longitudinal bars of the columns were extended up to the mid-depth of the slab and, at the bottom, were anchored in $1.5 \times 1.5 \times 0.35$ m³ concrete footings. The description of the slab casting procedure can be found in di Prisco et al.²⁷

The SFRC adopted had a mean cubic compressive strength at 28 days of 43.7 MPa, measured on five 150 mm-sided cubic specimens, which corresponds approximately to a C30/37 concrete class. Low-carbon hooked-end steel fibers with a length l_f of 60 mm and a

diameter d_f of 1.0 mm (aspect ratio $l_f/d_f = 60$) were added to the mix. A fiber content equal to 70 kg/m³ (0.89% by volume) was used. The material mix design, as well as the properties of the steel fibers, are given in di Prisco et al.²⁷

The post-peak tensile behavior of the material was determined through three-point bending tests on notched prismatic specimens having a cross-section of 150×150 mm², with a 25 mm-deep notch and a span of 500 mm, in accordance with the EN 14651²⁸ European Standard. For all the specimens, the limit of proportionality f_L and the residual flexural tensile strengths $f_{R(i)}$ at crack mouth opening displacements (CMOD) of 0.5, 1.5, 2.5, and 3.5 mm were measured. The residual strengths $f_{R(0.5)}$ and $f_{R(2.5)}$, respectively associated to CMODs of 0.5 and 2.5 mm, correspond to the values f_{R1} and f_{R3} introduced in the fib Model Code 2010¹⁰ to describe the FRC performance at serviceability and ultimate limit states of crack opening.

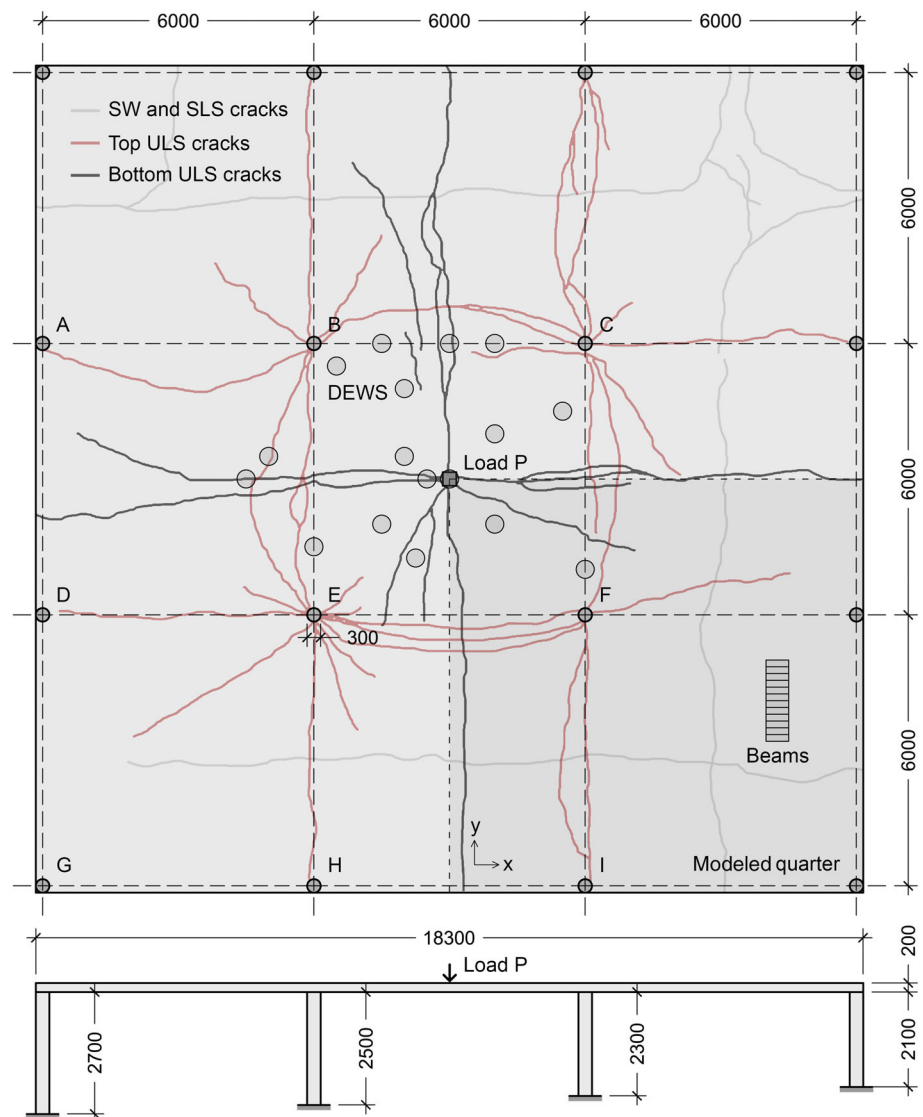


FIGURE 1 FRC flat slab geometry and reconstruction of the experimental crack patterns. Source: adapted from di Prisco et al.²⁷; nominal measures in mm

Nine prismatic notched specimens were cast on the same day of the slab (series C1), while 11 specimens were cast two days later (series C2, nominally identical to C1). Additional eight specimens (series C3) were extracted from an undamaged slab region (Figure 1), following the full-scale ULS test. The extracted specimens C3 were then notched on the face originally corresponding to the slab intrados and they had identical geometry to the cast specimens C1 and C2, apart the depth of 210 mm, over which a similar notch/depth ratio was maintained. The average strength characteristics, as well as the percent coefficients of variation (%CoV) of all the 28 notched beams (9 C1 + 11 C2 + 8 C3), are given in Table 1. For the sake of brevity, a complete discussion on the three-point bending test results for series C1–C3 is not reported here, but can be found in di Prisco et al.²⁷

The slab was initially tested at SLS,²⁶ imposing a uniformly distributed load of 4 kN/m² on panels A and C of Figure 1. The cracking developed due to the combined effect of shrinkage and self-weight (SW) at the removal of the formworks and at SLS is displayed in light gray and, given its limited interference with the ULS-induced pattern, is neglected in this study. The slab behavior at ULS was subsequently assessed by applying a concentrated load at the slab center, as schematically depicted in Figure 1. The cracking load was approximately equal to 85 kN, while the peak load was equal to 328 kN. The slab exhibited a remarkable plastic behavior, reaching more than 40 mm of deflection at the peak load. Bottom cracks along the median lines of the slab were observed, with the crack along the *y*-direction wider than the crack developed along the *x*-direction. The maximum crack opening recorded at the end of the test at the bottom of panel E was equal to 8.5 mm. The bottom cracks were followed by some radial cracks starting from the center of panel E. Radial cracks above the head of the internal columns and a large circular crack connecting the radial ones were observed on the top slab surface (Figure 1). Further details on the slab test setup and on the experimental results can be found in Parmentier et al.²⁶ and in di Prisco et al.²⁷

TABLE 1 Three-point bending test results on notched beam specimens C1, C2, and C3

	C1	C2	C3
Specimen No.	9	11	8
f_L (MPa)	5.1 (6.2%)	4.5 (11.0%)	4.2 (8.7%)
f_{R1} (MPa)	8.6 (19.0%)	6.4 (24.9%)	3.3 (23.8%)
f_{R3} (MPa)	7.5 (19.6%)	6.4 (20.3%)	3.5 (20.8%)

Note: Average values and, in round brackets, percent coefficient of variation (%CoV) reported.

3 | INVESTIGATED FRC TENSILE LAWS

The stress–strain relationships used in this study are all average multilinear tensile laws based on well-established proposals available in the literature. Figure 2 schematically shows a stress–strain law for a generic FRC softening material. It is composed by three branches (OA, AB, and BC) that describe the behavior of plain concrete in tension. The last part (branch CD) is related to the fiber pull-out mechanism.

The plain concrete behavior is described by a pre-peak stress–strain (σ_b , ϵ_t) response, followed by a stress–crack opening (σ_b , w) relationship based on the material fracture energy G_F . The three branches OA, AB, and BC are evaluated following two approaches available in literature:

- multilinear tensile law proposed by the *fib* Model Code 2010¹⁰ at §5.1.8.2;
- multilinear tensile law proposed by the *fib* Model Code 1990²⁵ at §2.1.4.4.2.

For the fiber pull-out branch, two proposals are considered:

- linear tensile law as proposed by the *fib* Model Code 2010¹⁰ at §5.6.4, in which the residual tensile strengths at the serviceability (f_{Fts}) and at the ultimate (f_{Ftu}) limit states are calculated as:

$$f_{Fts} = 0.45 \cdot f_{R1} \quad (1)$$

$$f_{Ftu} = 0.5 \cdot f_{R3} - 0.2 \cdot f_{R1} \quad (2)$$

- linear tensile law as proposed by di Prisco et al.,²³ back-calculated imposing sectional equilibrium at

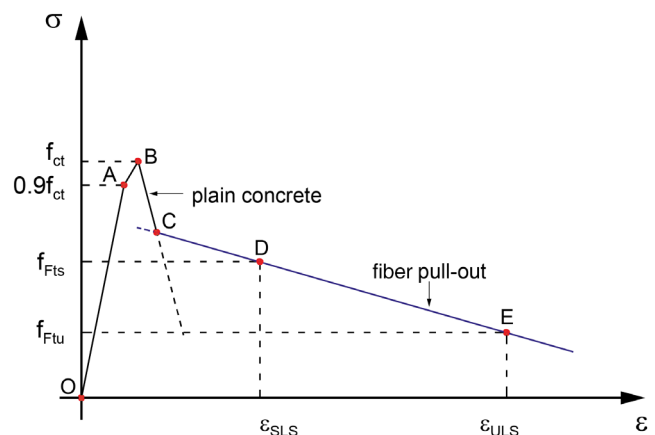


FIGURE 2 Schematic stress–strain relationship describing the softening behavior of FRC

0.5 and 2.5 mm of CMOD, in the hypotheses of (a) linear elastic behavior in compression at SLS; (b) compressive stress concentrated at the top fiber at ULS; and (c) simplified SLS and ULS tensile stress distributions over the cross-section. According to this approach, stresses f_{Fts} and f_{Ftu} are calculated as follows:

$$f_{Fts} = 0.37 \cdot f_{R1} \quad (3)$$

$$k_b = 0.529 - 0.143 \cdot (f_{R3}/f_{R1}) \quad (4)$$

$$f_{Ftu} = 0.5 \cdot f_{R3} - \left(\frac{k_b}{2} \cdot f_{R1} \right) \quad (5)$$

It is worth noting that, since all the calculated f_{Fts} are smaller than the average uniaxial tensile strength of plain concrete f_{ct} , point C in Figure 2 always results from the intersection of the fiber pull-out branch with the unstable propagation branch of plain concrete. Relevant mechanical tensile parameters of the investigated FRC are listed in Table 2. Note that the values of the residual tensile strengths f_{Fts} and f_{Ftu} reported in Table 2 are calculated using the average data f_{R1} and f_{R3} derived from the prismatic notched beams directly extracted from the slab (series C3 in Table 1), assumed the most representative, even if in many samples no rotation in relation to the cast direction was applied to the specimens (as specified in the EN 14651) and therefore any contribution due to fiber sedimentation on the bottom, carefully analyzed in di Prisco et al.,²³ is neglected. It is worth noting that the average residual strengths f_{R1} and f_{R3} of series C3 (extracted from the slab) are in line with the characteristic values of set C2 (specifically produced for classification purposes)²⁹ and this is justified by the reduced number of fibers counted on the ligament section of specimens C3.²³

Six different tensile constitutive laws are then built, combining the proposals (i)–(iv) as described below.

1. Tensile law n.1: a multilinear tensile law built using the proposals of *fib* Model Code 2010¹⁰ for both the pre-peak—approach (i)—and post-peak branches—approach (iii)—.
2. Tensile law n.2: branches OA, AB, and BC related to plain concrete are evaluated following the proposal of

fib Model Code 2010¹⁰—approach (i)—, whilst the fiber pull-out branch is evaluated with the proposal of di Prisco et al.²³—approach (iv)—.

3. Tensile law n.3: a multilinear tensile law similar to the law n.1, with the exception that the pre-peak law is linear, instead of bilinear (i.e., point A coincides with point B in Figure 2).
4. Tensile law n.4: a multilinear tensile law similar to the law n.2, with the exception that pre-peak law is assumed linear, instead of bilinear (i.e., point A coincides with point B in Figure 2).
5. Tensile law n.5: a multilinear tensile law similar to the law n.2, with the exception that f_{ct} is back-calculated from the notched beam flexural data at the limit of proportionality (f_L in Table 1).
6. Tensile law n.6: plain concrete law evaluated according to the *fib* Model Code 1990²⁵—approach (ii)—with a pre-peak linear law (i.e., point A coincides with point B in Figure 2). The fiber pull-out branch is evaluated according to the proposal of di Prisco et al.²³—approach (iv)—.

The significant values of the obtained stress-strain/stress-crack opening tensile laws 1–6 are collected in Table 3 and displayed in Figure 3.

4 | NUMERICAL FE MODELS

The numerical models of the FRC notched beams and of the FRC flat slab are built and processed by employing the software Abaqus 6.14-5.³⁰ Material and geometric characteristics of the FE models are described in the following subsections.

4.1 | Basic material parameters

FRC elastic properties are derived from the *fib* Model Code 2010¹⁰ and listed in Table 4. The material inelastic behavior was simulated by means of the Concrete Damaged Plasticity (CDP) model, based on the biaxial yield function originally developed by Lubliner et al.³¹ and later modified by Lee and Fenves.³²

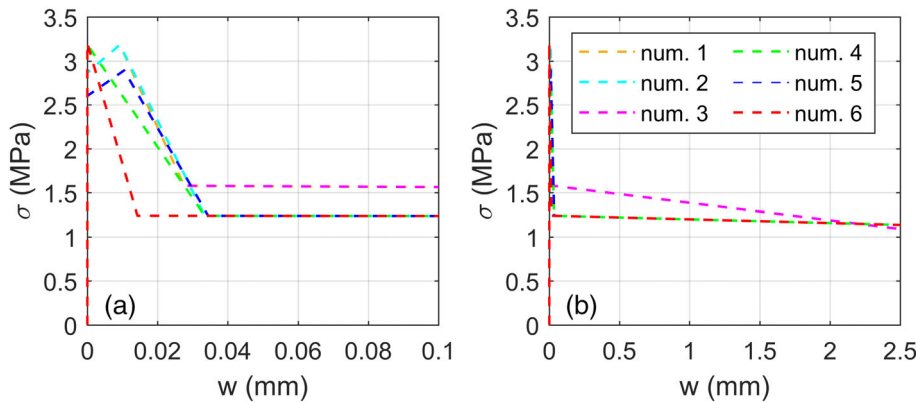
In the numerical analyses presented in this study, damage is not accounted and the simulations are therefore

TABLE 2 Relevant mechanical tensile parameters of the investigated FRC (average values)

	<i>fib</i> Model Code 1990 ²⁵	<i>fib</i> Model Code 2010 ¹⁰	di Prisco et al. ²³
f_{ct} (MPa)	3.20	3.18	–
G_F (N/m)	69.46	139.33	–
f_{Fts} (MPa)	–	1.485	1.221
f_{Ftu} (MPa)	–	1.090	1.137

TABLE 3 Multilinear stress-strain/stress-crack opening tensile behavior: laws 1–6 considered in the numerical analyses

Law n. 1			Law n. 2			Law n. 3		
σ_t (MPa)	ϵ_t (–)	w (mm)	σ_t (MPa)	ϵ_t (–)	w (mm)	σ_t (MPa)	ϵ_t (–)	w (mm)
0	0	–	0	0	–	0	0	–
2.87	8.83E–05	–	2.87	8.83E–05	–	3.18	9.81E–05	0
3.18	1.50E–04	0	3.18	1.50E–04	0	1.58	–	2.76E–2
1.58	–	2.76E–2	1.24	–	3.34E–2	1.49	–	0.5
1.49	–	0.5	1.22	–	0.5	1.09	–	2.5
1.09	–	2.5	1.14	–	2.5	–	–	–
Law n. 4			Law n. 5			Law n. 6		
σ_t (MPa)	ϵ_t (–)	w (mm)	σ_t (MPa)	ϵ_t (–)	w (mm)	σ_t (MPa)	ϵ_t (–)	w (mm)
0	0	–	0	0	–	0	0	–
3.18	9.81E–05	0	2.60	8.02E–05	–	3.20	9.86E–05	0
1.24	–	3.34E–02	2.89	1.50E–04	0	1.24	–	1.43E–02
1.22	–	0.5	1.24	–	3.44E–02	1.22	–	0.5
1.14	–	2.50	1.22	–	0.5	1.14	–	2.50
–	–	–	1.14	–	2.50	–	–	–

**FIGURE 3** Multilinear stress-crack opening tensile laws considered in the numerical analyses: (a) zoom in the crack opening range 0–0.1 mm and (b) full plot**TABLE 4** Basic material properties (E_{ci} : tangent modulus of elasticity; ν : Poisson coefficient; ρ : density) and plasticity parameters of the CDP model adopted for the FRC notched beams and the FRC flat slab (ψ : dilation angle; ϵ : flow potential eccentricity; σ_{b0}/σ_{c0} : ratio between the biaxial and the uniaxial compression strengths; K_c : Drucker–Prager surface modifier; ξ : viscosity parameter)

Parameter	Value
E_{ci} (MPa)	32,474
ν (–)	0.2
ρ (kg/m ³)	2,290
ψ (°)	13
ϵ (–)	0.1
σ_{b0}/σ_{c0} (–)	1.16
K_c (–)	0.667
ξ (–)	1×10^{-5}

based on a fully elasto-plastic material response, both in tension and compression. The adopted plasticity parameters such as the dilation angle ψ , the flow potential eccentricity ϵ , the ratio between the initial equibiaxial compressive yield stress and the initial uniaxial compressive yield stress σ_{b0}/σ_{c0} and the Drucker–Prager surface modifier K_c are those suggested in the literature for plain concrete.³³ The adopted parameters of the CDP model are listed in Table 4.

To reduce numerical convergence issues, a viscoplastic regularization of the constitutive equations is adopted by employing a viscosity parameter ξ . The value of the viscosity parameter (Table 4) is set equal to 1×10^{-5} , to limit any macroscopic alteration of the numerical results.

Material nonlinearity is accounted providing to the software a nonlinear stress-strain (σ_c – ϵ) law in compression and piecewise-linear stress-crack opening (σ_t – w)

TABLE 5 Relevant mechanical parameters of the investigated FRC identified according to the *fib* Model Code 2010¹⁰ and the *fib* Model Code 1990²⁵ (average values)

Average parameter	MC2010	MC1990
Cylindrical compressive strength f_c (MPa)	36.3	–
Peak compressive strain ε_{c1} (–)	–2.3‰	–
Ultimate compressive strain $\varepsilon_{c,lim}$ (–)	–3.5‰	–
Tensile strength f_{ct} (MPa)	3.18	3.20
Fracture energy G_F (N/m)	139.33	69.46

laws in tension. Relevant average mechanical parameters of the investigated FRC identified according to the directions given by the *fib* Model Code 2010,¹⁰ or by the *fib* Model Code 1990,²⁵ are listed in Table 5.

The average compressive strength value (f_c) reported in Table 5 is used to determine the compressive constitutive laws of FRC. This last is described by the nonlinear curve proposed by the *fib* Model Code 2010¹⁰:

$$\sigma_c = -f_c \left(\frac{k \cdot \eta - \eta^2}{1 + (k-2) \cdot \eta} \right) \text{ for } |\varepsilon_c| \leq |\varepsilon_{c,lim}| \quad (6)$$

where η is the normalized strain ratio $\varepsilon_c/\varepsilon_{c1}$ and k is the ratio between the tangent elastic modulus and the secant elastic modulus at the peak stress.

Since the employed software does not allow the simultaneous introduction of mixed stress–strain and stress-displacement uniaxial behaviors, the multilinear tensile laws described in §3 and summarized in Table 3 are entirely converted into stress-displacement tensile laws by multiplying the inelastic components of the tensile strains at point B (Figure 2, in case of laws 1, 2, and 5) by a numerical characteristic length, assumed equal to the average mesh size of the investigated model. This last is equal to 2.5 and 150 mm for the two-dimensional (2D) numerical models of the notched beams and the flat slab, respectively. An automatic pseudo-regularization based on mode I fracture energy, originally developed for plain concrete, is finally adopted by the software and, to avoid numerical issues, the last linear branches of the tensile and compressive laws are extended down to a roughly null stress level.

4.2 | Notched beams

Four-node bilinear quadrilateral isoparametric plane stress elements (CPS4R) with reduced integration and hourglass control are employed to discretize the notched beams. A structured mesh with an average mesh size

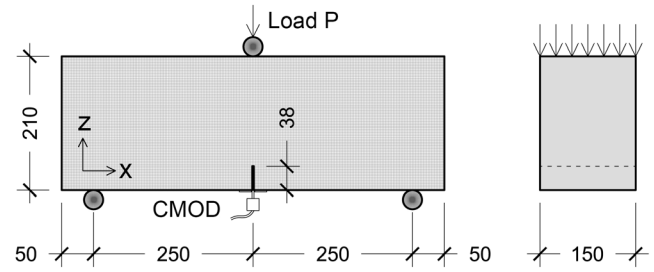


FIGURE 4 View of the mesh adopted for the notched beams (measures in mm)

equal to $2.5 \times 2.5 \text{ mm}^2$ is considered (Figure 4). According to the experimental setup used, the supporting and the loading rollers are also modeled and a contact is introduced at the beam/roller interfaces, considering: (i) a “hard” normal behavior in the z direction, and (ii) a “penalty” tangential behavior in the x direction, controlled by a friction coefficient of 0.5. The simulations are displacement controlled by imposing an increasing vertical displacement at the center point of the loading knife, using a Static-General step numerically solved with the Full Newton technique.³⁰

4.3 | Full-scale flat slab

In this paragraph, the description of the finite element modeling of the FRC full-scale flat slab tested by Parmen-tier et al.²⁶ is reported. Finite element analyses are carried out by considering mechanical nonlinearities, evaluated by adopting the CDP model described in §4.1. Given the objective of this study and the maximum out-of-plane displacement of about 1/3 of the slab thickness, geometrical nonlinearity is neglected.

2D and three-dimensional (3D) modeling strategies are employed to discretize the slab. The symmetry of loading and boundary conditions allows to model only a quarter of the FRC slab (Figure 1). In doing this, the height differences in the columns are assumed to have negligible impact on the structural response under vertical loads.

The 2D models are discretized with 4-node shell elements (S4) having an average mesh size equal to 150 mm. The mesh is refined in the load introduction region, imposing a local average mesh size of 100 mm. Four integration points over the reference plane and six degrees of freedom (DOF) per node characterize the shell element. Five integration points based on the Simpson integration rule are used over the thickness, assumed equal to 210 mm (as measured on-field).

The 3D model is instead discretized with 8-node linear hexahedron elements with 3 DOFs per node

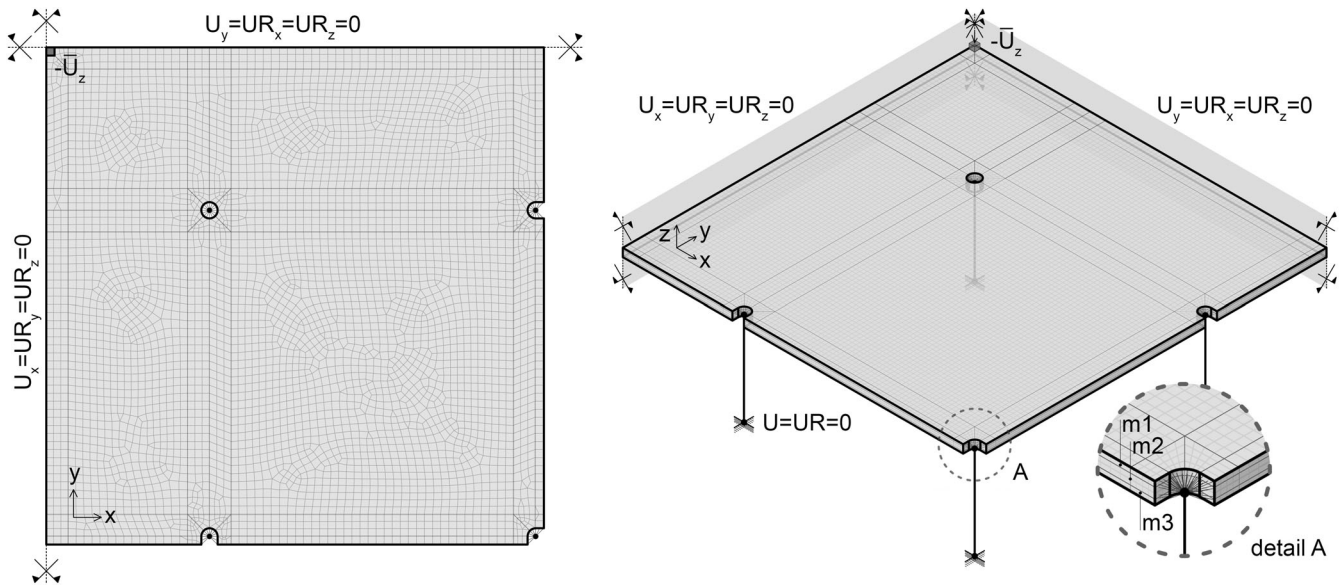


FIGURE 5 Representation of the meshes adopted in modeling the selected quarter of the FRC flat slab: shell elements (left) and brick elements (right)

(C3D8R). An average mesh size of 100 mm is used on the slab's plane, while along the thickness four elements are adopted, resulting in an average mesh size in the z direction equal to 52.5 mm.

All slab models are supported by a set of columns modeled with linear beam elements with 2 nodes and 6 DOF per node (B31) with an average mesh size of 200 mm. The behavior of the columns is assumed elastic and the two ends are respectively fixed at the bottom node, and connected to the slab at the top node through a “structural distributing” coupling selected to avoid unphysical stress concentrations (see detail A of Figure 5). The stresses associated to the self-weight are accounted introducing a gravity step, and the effects of concrete shrinkage are also included, imposing to the slab a uniform strain $\varepsilon_{sh} = -7.63E-5$. This value corresponds to the combined autogenous and drying components exhibited by the employed concrete at 42 days of age at a relative humidity of 80%, with only the top surface in direct contact with the atmosphere.¹⁰ Note that this approach represents a first approximation, as in reality non-uniform shrinkage strains are developed over the slab section, and might result in additional damage entailed to the time evolution of material strength.

The ULS load is finally applied at the slab center, imposing a vertical downward displacement ($-\bar{U}_z$) on an area of $300 \times 300 \text{ mm}^2$ (according to the test setup) through a Static-General step.³⁰ Displacement controlled analyses are carried out in the application of the vertical load to overcome numerical instabilities associated with the development of short softening slab responses.

Translational and rotational boundary conditions are assigned along the symmetry edges (Figure 5). In particular, displacements along the y -axis and rotations are restrained at the symmetry edge parallel to the x -direction ($U_y = 0$; $UR_x = UR_z = 0$). Similar boundary conditions are assigned to the symmetry edge parallel to the y -direction ($U_x = 0$; $UR_y = UR_z = 0$). The main characteristics of the FE models adopted to simulate the FRC flat slab are summarized in Table 6.

5 | NUMERICAL RESULTS

5.1 | Implications on the selection of the FRC tensile law

The following sub-sections aim at exploring the capability of a commercial nonlinear finite element software in simulating the responses of FRC notched beams, analyzing the role of the multiple uniaxial tensile laws discussed in §3. In a second step, the study evaluates whether the numerical-experimental differences observed on the notched beams are conserved, amplified, or reduced on the analysis of the full-scale FRC flat slab.

5.1.1 | Notched beams

Figure 6 shows the average nominal stress σ_N versus CMOD curve derived from the three-point bending tests (C3 series), together with the numerical FE results. The

TABLE 6 Main characteristics of the FE models adopted to simulate the FRC flat slab

FE model ID	Model type	Tensile law ID	Material heterogeneity over the thickness
num. 1	2D	1	No
num. 2	2D	2	No
num. 3	2D	3	No
num. 4	2D	4	No
num. 5	2D	5	No
num. 6	2D	6	No
num. 7	3D	6	No
num. 8	3D	6	Yes

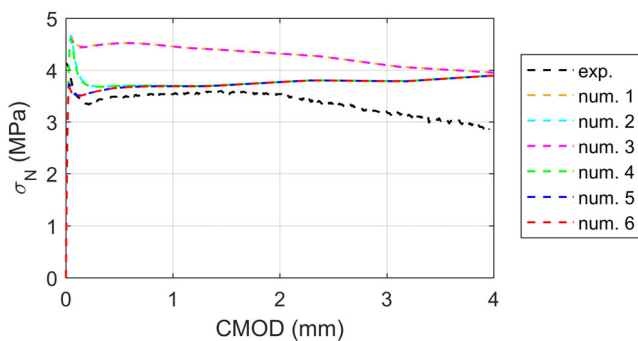


FIGURE 6 Comparison between the experimental (C3 series) and the FE analysis results for the FRC notched beams

results of the six nonlinear models detailed in Table 3 and labeled as num. 1–num. 6 are compared with the average experimental data. Analyzing the results of Figure 6, several remarks can be drawn.

First, as highlighted by a recent study,³⁴ the influence of the type of the pre-peak branch—linear or bilinear—on the response of the notched beams appears marginal, as can be observed by comparing the responses num. 1 with num. 3 and num. 2 with num. 4. In practical situations in which a detailed modeling of the fracture process zone is beyond the scope, this observation is considered relevant, as many modeling software only allow the introduction of uniform stress–strain or stress–displacement tensile laws and might lead to potential errors in the adaption of the multilinear material behavior. As a result, the linearization of the pre-peak branch up to f_{ct} allows to describe the whole tensile response only with a stress–displacement post-cracking relationship and a correct energy dissipation per unit area is guaranteed by simple regularization procedures.

With reference to the post-peak branch associated with the fiber pull-out, the numerical analyses obtained adopting

the indications given by *fib* Model Code 2010¹⁰—responses num. 1 and num. 3—provide an overestimation of the experimental response, both in the SLS and ULS ranges. The numerical responses obtained using the proposal of di Prisco et al.²³—responses num. 2 and num. 4—provide a better prediction of the experimental data, being developed on the basis of more precise sectional equilibrium equations. However, all the mentioned analyses overestimate the peak nominal stress for small values of CMOD.

Analyses num. 2 and num. 5 differ only in how f_{ct} is calculated: from the compressive strength the first ($f_{ct} = 3.18$ MPa) through empirical formulas, and from the flexural tensile strength f_L of the notched beams the second ($f_{ct} = 2.89$ MPa), considering a ligament depth of 172 mm. As expected, analysis num. 5, which uses a lower value of f_{ct} , provides a lower peak stress value than analysis num. 2. For values of CMODs greater than 0.5 mm, the two responses are almost identical, as the effect of the adopted tensile cracking stress becomes increasingly limited.

The numerical analysis that best reproduces the experimental data, given a fixed f_{ct} calculated from the peak compressive strength (as frequently happens in common practice), is that labeled as num. 6. Compared to analysis num. 4, it adopts the formulation proposed by the *fib* Model Code 1990²⁵ for the description of plain concrete, while both analyses num. 4 and num. 6 use the proposal of di Prisco et al.²³ for the description of the fiber pull-out branch. As expected, analyses num. 4 and num. 6 only differ for values of CMODs lower than 0.4 mm. This is explained by the important impact of the slope of the descending branch of the plain concrete strain-softening diagram (BC in Figure 2) on the flexural response of the beam cross-section³⁵; as displayed in Table 2, the fracture energy G_F provided by the *fib* Model Code 1990²⁵ is about 50% of that proposed by the *fib* Model Code 2010,¹⁰ with obvious implications on the brittleness of the unstable propagation branch associated to plain concrete. This, in turn, results in a marked alteration of the beam numerical response, given the introduced sectional redundancy. For CMODs greater than about 2 mm analyses num. 2, num. 4, num. 5, and num. 6 overestimate the experimental results, as the extension of the last branch of the tensile law, combined with the reduced slope of the pull-out branch, involves an overestimation of the crack opening at zero residual tensile stress.

5.1.2 | Full-scale flat slabs

Figure 7 presents the experimental and numerical load–central deflection relationships (P – δ). As general remark,

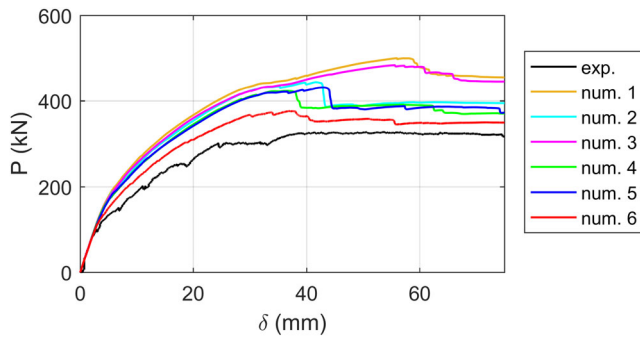


FIGURE 7 Comparison between the experimental and the FE analysis results for the FRC flat slab

the modeling implications observed in the notched beams are substantially maintained in the FRC flat slab. In particular, FE models that largely over-predicted the notched beam response (i.e., models num. 1 and num. 3) provide the largest overestimation of the flat slab response, furtherly amplified by the introduction of redundancies at the structural level. The benefits given by the use of the tensile law of di Prisco et al.²³ in place of that proposed by the *fib* Model Code 2010¹⁰ for the description of the fiber pull-out branch are clearly visible in Figure 7 (see num. 1, num. 3 vs. num. 2, num. 4). The overestimation of the ultimate experimental load calculated for a central displacement of 80 mm passes from +45% to +20% for analyses num. 3 and num. 4, respectively.

The use of a linear or bilinear pre-peak law has a limited influence on the response of the slab, as already highlighted in the discussion of the notched beams (see the comparison between analyses num. 1 and num. 3 and between num. 2 and num. 4).

In the flat slab the first marked loss of stiffness, accompanied by the formation of a major crack, was experimentally observed at a load of about 85 kN. Numerical models num. 1–num. 5, which share similar plain concrete post-peak tensile behaviors, largely overestimate the cracking load. On the other hand, it can be noticed that the model num. 6, which adopts the formulation proposed by the *fib* Model Code 1990²⁵ to derive the tensile law to be associated to plain concrete, captures with suitable accuracy the pre- and post-cracking behaviors of the slab. Model num. 6 overestimates the experimental cracking load by about +20% and the ultimate experimental load by about +12%.

The experimental crack pattern of the slab at the end of the ULS test²⁶ is compared in Figure 8 with the numerical tensile equivalent plastic strains (PEEQT) at a midspan deflection δ equal to 80 mm. For such large midspan displacements, the crack patterns provided by the numerical analyses num. 1–num. 6 appear very similar. In the following, the evolution of the crack pattern of

the model that best reproduces the global response of the slab, num. 6, is discussed.

As documented by the experimental test, prior to the application of the ULS load the slab was already cracked at some locations, due to the action exerted by the self-weight at the early removal of formworks. Since a time-independent material strength is adopted in this work, the effect of gravitational loads and shrinkage only results in limited plastic strains at the columns locations. In the numerical model num. 6, the first considerable cracks appear on top center columns and progressively propagate along with the alignments of the inner columns. At the bottom side, cracks in the numerical model num. 6 appear due to positive bending moments and develop into two directions parallel to the slab edges along the median lines, consistently with the experimental observations (Figures 1 and 8). Note that bottom median cracks are poorly represented in Figure 8, since only a quarter of the whole FRC slab is modeled and the resulting plastic strain maps are mirrored about the xz and yz planes for clarity of exposition. On the extrados face, FE model num. 6 satisfactorily reproduces the large circular crack connecting the inner columns, but fails in following the propagation of radial diagonal cracks, likely due to the structured nature of the adopted meshes (Figure 8).

Based on the results reported in this section, it can be stated that the model labeled as num. 6 satisfactorily reproduces the mechanical response of the FRC flat slab in terms of global response (load–deflection relation) and is able to capture with a quite good approximation the regions in which the irreversible strains induced by cracking localize, even if it neglects completely the heterogeneity of the material experimentally identified.²⁷

5.2 | Role of numerical modeling choices on the response of FRC flat slabs

In the previous section, the implications of the choice of the constitutive tensile law on the structural response of FRC notched beams and FRC full-scale flat slabs were examined. Two further aspects are considered in this section concerning the role of numerical modeling choices on the structural response of FRC flat slabs:

- influence of the adoption of shell (model num. 6 in Table 6) or brick elements (model num. 7 in Table 6) in the numerical modeling;
- influence of the material homogeneity (models num. 6 and num. 7 in Table 6) or heterogeneity (model num. 8 in Table 6) in the slab thickness.

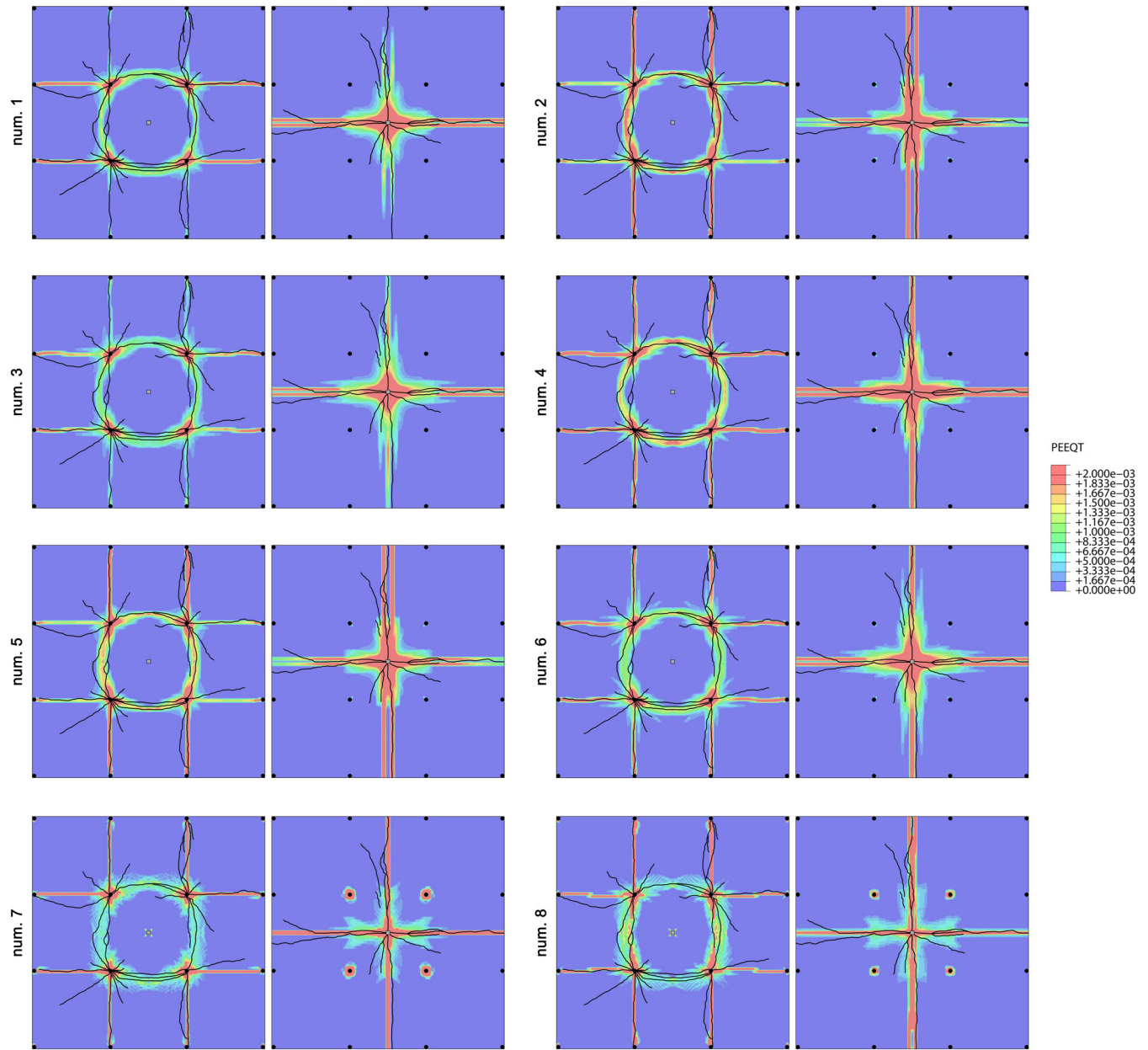


FIGURE 8 Crack patterns (experimental) and contours of the tensile equivalent plastic strains (PEEQT) at the top and bottom faces of numerical models num.1–num. 8. Please note that the one-fourth PEEQT maps are mirrored about the xz and yz planes for clarity of exposition and equivalent plastic strains greater than $2E-03$ are uniformly displayed in red

TABLE 7 Multilinear stress-crack opening laws accounting for material heterogeneity over the slab cross-section

m1 $\beta_1 = 0.65$ $\beta_2 = 0.46$		m2 (law n. 6) $\beta_1 = 1.0$ $\beta_2 = 1.0$		m3 $\beta_1 = 1.32$ $\beta_2 = 1.04$	
σ_t (MPa)	w (mm)	σ_t (MPa)	w (mm)	σ_t (MPa)	w (mm)
3.20	0	3.20	0	3.20	0
0.90	$1.68E-02$	1.24	$1.43E-02$	1.78	$1.04E-02$
0.79	0.5	1.22	0.5	1.61	0.5
0.36	2.5	1.14	2.5	0.94	2.5

In order to correctly examine the effects described above, the numerical models num. 6–num. 8 share the same constitutive law, chosen as the best performing in

the previous section. Material heterogeneity is introduced imposing three different materials m1, m2, and m3 over the slab thickness (detail A in Figure 5).

Material m2 corresponds to law n. 6 in Table 3, and is assigned to the central half of the slab section. Materials m1 and m3, respectively assigned to the top and bottom quarters of the section depth, are defined based on the results obtained in di Prisco et al.²⁷ from the double edge wedge splitting (DEWS) specimens cored after the ULS test at multiple locations (Figure 1). Fiber segregation is reflected in a set of modification coefficients β_1 and β_2 , respectively applied to the f_{R1} and f_{R3} residual strengths of Table 1 (case C3), while keeping constant the plain concrete parameters (f_{ct} and G_F); the resulting multilinear tensile laws are reported in Table 7. The effect of the distribution of fibers along the depth of the slab cross section on the response of

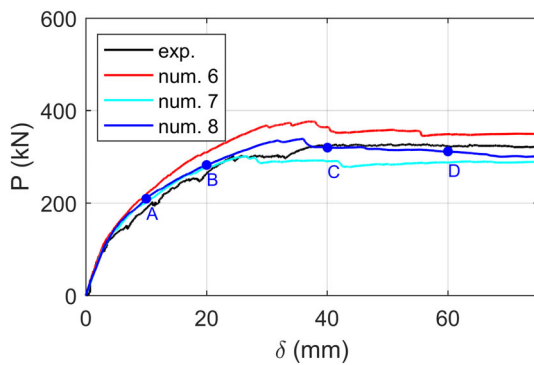


FIGURE 9 Effect of the numerical kinematic discretization (2D vs. 3D) and of the cross-sectional material heterogeneity on the slab response

FRC elevated slabs was also numerically studied by Salehian and Barros.³⁶

Figure 9 compares the experimental and numerical (num. 6–num. 8) load–central deflection relationships (P – δ). The role played by the kinematic discretization of the slab (2D vs. 3D) and by the material heterogeneity appears relevant (Figure 9). The most refined model (num. 8), which includes both a 3D kinematic discretization and the heterogeneity of the material along the slab thickness, is the one that best reproduces the experimental response.

Both 3D models num. 7 and num. 8 better reproduce, compared to the 2D model, all the post-cracking stages up to the ultimate load reached by the slab. The better performance of the 3D models is also justified by an improved reproduction of the crack patterns (Figure 8). The comparison among the tensile equivalent plastic strains of numerical models num. 6 and num. 8 (Figure 8) highlights how in the 2D model the plastic strains are smeared over a wider area. This leads to both (i) a delayed activation of the first cracking and (ii) an overestimation of the global behavior of the slab.

The evolution of tensile equivalent plastic strains (PEEQT) in the top and bottom faces of numerical model num. 8 is presented in Figure 10. Points A–D in Figure 10 refer to different events in the load–central deflection response (Figure 9). Initially, cracks appear around the top of the center columns and at the bottom of the slab center (point A). Subsequently, the bottom cracks propagate in two directions parallel to the slab

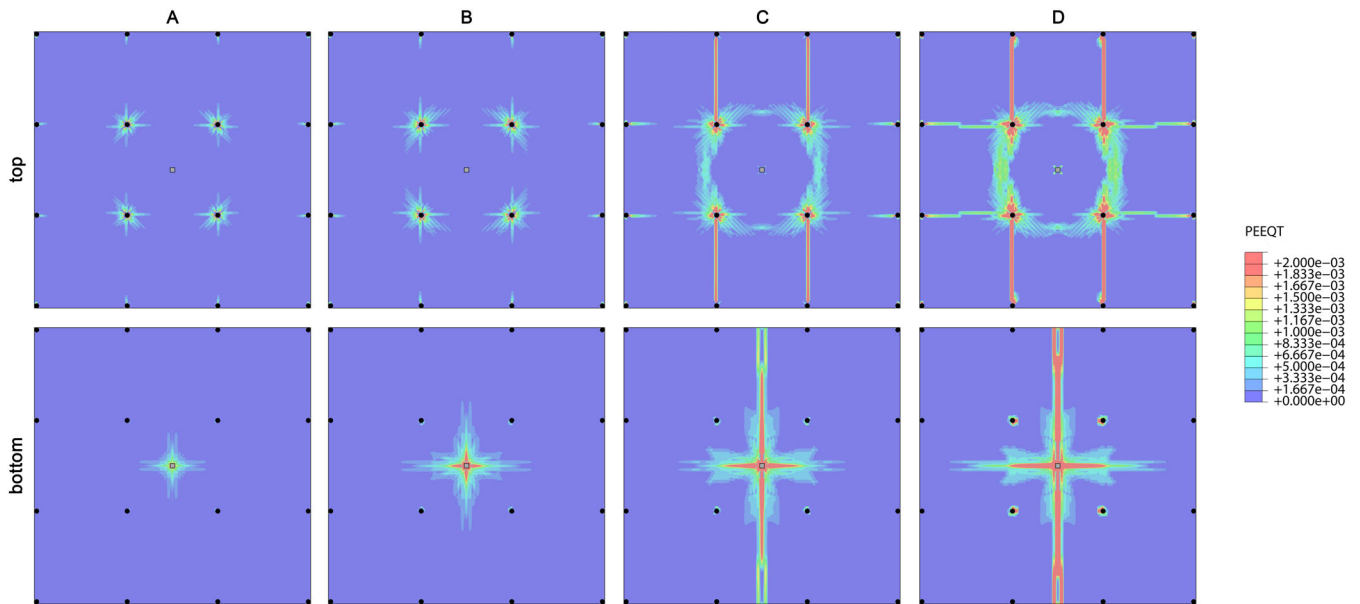


FIGURE 10 Evolution of tensile equivalent plastic strains (PEEQT) at the top and bottom faces of numerical model num. 8 at points A, B, C, and D on the diagram of FIGURE 9. Please note that the one-fourth PEEQT maps are mirrored about the xz and yz planes for clarity of exposition and equivalent plastic strains greater than $2E-03$ are uniformly displayed in red

edges, along the median lines (point B). Then, at the top side, cracks grow along the alignments of the inner columns and a large circular crack is developed above the internal group of columns. At the bottom side, a crack along one median line is completely formed (point C). Finally, the cracks width increases, as witnessed by the larger values of tensile equivalent plastic strains (point D).

As a closing note, the simulation performances of the constitutive approaches presented in this work must be generalized with caution, as the stress fields developed in real structures can be strongly influenced by the boundary conditions and by time-dependent phenomena such as shrinkage and strength development over curing time. Furthermore, the specific shape of the FRC uniaxial tensile law could entail unexpected numerical outcomes that should be controlled through tailored validation procedures. To this aim, future developments may include extending the proposed approach to flat slabs characterized by different geometries, hybrid solutions (fibers + ordinary reinforcement) and structures manufactured with different FRC classes.

6 | CONCLUSIONS

Based on the discussed results related to FRC flat slabs, it is possible to draw the following conclusions:

- the choice of the tensile constitutive law among those most commonly used both in research and in the design practice can lead to relevant differences in the numerical results.
- Small-to-moderate dispersion of the numerical results of the notched FRC beams due to the adoption of different tensile laws can be amplified in the simulation of FRC elevate slabs, due to their inherent structural redundancy. Larger dispersions of the numerical results could be expected in presence of FRCs in which the structural response is dominated by the pull-out branch (i.e., strain-hardening materials and composites in which the residual tensile values are comparable with the first cracking strength).
- The influence of the type of pre-peak tensile law (linear or bilinear) associated to plain concrete on the response of FRC notched beams and FRC flat slabs is marginal, in particular in the cases in which a detailed description of the fracture mechanics is not required. This observation may be relevant, in light of the fact that many software employed by structural designers do not allow the introduction of mixed stress-strain and stress-displacement laws.

- In modeling strain-softening FRCs, the fracture energy associated to plain concrete might play an important role. The adoption of a conservative value of G_F results in a steeper descending branch of the plain concrete strain-softening diagram, with clear implications on the numerical response at the sectional and structural scales, in particular in the immediate post-localization phase.
- The role played by the slab kinematic discretization (shell vs. brick elements) and by the homogeneity versus heterogeneity of the material along with the slab thickness is also relevant, as shown by the comparison between the experimental and the numerical results. More advanced numerical approaches could also include in-plane material heterogeneity.

CONFLICT OF INTEREST

No potential conflict of interest was reported by the authors.

DATA AVAILABILITY STATEMENT

The data that support the findings of this study are available from the corresponding author upon reasonable request.

ORCID

Giulio Zani  <https://orcid.org/0000-0001-9794-7820>

Paolo Martinelli  <https://orcid.org/0000-0003-1029-7744>

Marco di Prisco  <https://orcid.org/0000-0003-1779-2449>

REFERENCES

1. di Prisco M, Plizzari G, Vandewalle L. Fibre reinforced concrete: new design perspectives. *Mater Struct Constr*. 2009;42(9):1261–81. <https://doi.org/10.1617/s11527-009-9529-4>
2. Belletti B, Cerioni R, Meda A, Plizzari G. Design aspects on steel fiber-reinforced concrete pavements. *J Mater Civ Eng*. 2008;20(9):599–607. [https://doi.org/10.1061/\(asce\)0899-1561\(2008\)20:9\(599\)](https://doi.org/10.1061/(asce)0899-1561(2008)20:9(599))
3. Alani AM, Beckett D. Mechanical properties of a large scale synthetic fibre reinforced concrete ground slab. *Construct Build Mater*. 2013;41:335–44. <https://doi.org/10.1016/j.conbuildmat.2012.11.043>
4. Meda A, Plizzari GA, Riva P. Fracture behavior of SFRC slabs on grade. *Mater Struct Constr*. 2004;37(270):405–11. <https://doi.org/10.1617/14093>
5. Jamshidi Avanaki M, Hoseini A, Vahdani S, de Santos C, de la Fuente A. Seismic fragility curves for vulnerability assessment of steel fiber reinforced concrete segmental tunnel linings. *Tunn Undergr Sp Technol*. 2017;2018(78):259–74. <https://doi.org/10.1016/j.tust.2018.04.032>
6. de la Fuente A, Pujadas P, Blanco A, Aguado A. Experiences in Barcelona with the use of fibres in segmental linings. *Tunn Undergr Sp Technol*. 2012;27:60–71. <https://doi.org/10.1016/j.tust.2011.07.001>

7. Chiaia B, Fantilli AP, Vallini P. Combining fiber-reinforced concrete with traditional reinforcement in tunnel linings. *Eng Struct*. 2009;31:1600–6. <https://doi.org/10.1016/j.engstruct.2009.02.037>
8. de la Fuente A, Aguado A, Molins C, Armengou J. Innovations on components and testing for precast panels to be used in reinforced earth retaining walls. *Construct Build Mater*. 2011; 25(5):2198–205. <https://doi.org/10.1016/j.conbuildmat.2010.11.003>
9. de la Fuente A, Escariz RC, De Figueiredo AD, Aguado A. Design of macro-synthetic fibre reinforced concrete pipes. *Construct Build Mater*. 2013;43:523–32. <https://doi.org/10.1016/j.conbuildmat.2013.02.036>
10. fib. fib Model Code for Concrete Structures 2010, Lausanne; 2013.
11. Martinelli P, Colombo M, de la Fuente A, Cavalaro S, Pujadas P, di Prisco M. Characterization tests for predicting the mechanical performance of SFRC floors: design considerations. *Mater Struct Constr*. 2021;54(1):1–16. <https://doi.org/10.1617/s11527-020-01598-2>
12. Hedebratt J, Silfwerbrand J. Full-scale test of a pile supported steel fibre concrete slab. *Mater Struct Constr*. 2014;47(4):647–66. <https://doi.org/10.1617/s11527-013-0086-5>
13. Salehian H, Barros JAO. Assessment of the performance of steel fibre reinforced self-compacting concrete in elevated slabs. *Cem Concr Compos*. 2015;55:268–80. <https://doi.org/10.1016/j.cemconcomp.2014.09.016>
14. di Prisco M, Colombo M, Pourzarabi A. Biaxial bending of SFRC slabs: is conventional reinforcement necessary? *Mater Struct Constr*. 2019;52(1):1–15. <https://doi.org/10.1617/s11527-018-1302-0>
15. Nogales A, de la Fuente A. Numerical-aided flexural-based design of fibre reinforced concrete column-supported flat slabs. *Eng Struct*. 2020;2021(232):111745. <https://doi.org/10.1016/j.engstruct.2020.111745>
16. di Prisco M, Sibaud F, Failla C, et al. Innovative SFRC applications: an industrial building in Como. In: di Prisco M, Menegotto M, editors. *Proceedings of Italian concrete days*. Lecco (Italy); Italy: GWMAX s.r.l.; 2018. p. 273–82.
17. Aidarov S, Mena F, de la Fuente A. Structural response of a fibre reinforced concrete pile-supported flat slab: full-scale test. *Eng Struct*. 2021;239:112292. <https://doi.org/10.1016/j.engstruct.2021.112292>
18. ACI 544.6R-15. Report on Design and Construction of Steel Fiber-Reinforced Concrete Elevated Slabs; 2015.
19. ACI 544.4R-88. Design Considerations for Steel Fiber Reinforced Concrete; 1988.
20. RILEM TC 162-TDF. Final recommendation of RILEM TC 162-TDF: test and design methods for steel fibre reinforced concrete sigma-epsilon-design method. *Mater Struct Constr*. 2003;36:560–7. <https://doi.org/10.1007/BF02480834>
21. CNR-DT 204/2006. Guidelines for the design, construction and production control of fibre reinforced concrete structures; 2008.
22. Amin A, Foster SJ, Muttoni A. Derivation of the σ - w relationship for SFRC from prism bending tests. *Struct Concr*. 2015; 16(1):93–105. <https://doi.org/10.1002/suco.201400018>
23. di Prisco M, Colombo M, Dozio D. Fibre-reinforced concrete in fib model code 2010: principles, models and test validation. *Struct Concr*. 2013;14(4):342–61. <https://doi.org/10.1002/suco.201300021>
24. Gao D, Ding C, Pang Y, Chen G. An inverse analysis method for multi-linear tensile stress-crack opening relationship of 3D/4D/5D steel fiber reinforced concrete. *Construct Build Mater*. 2021;309(97):125074. <https://doi.org/10.1016/j.conbuildmat.2021.125074>
25. CEB-FIP. CEB-FIP Model Code 90; 1993.
26. Parmentier B, Van Itterbeeck P, Skowron A. The behaviour of SFRC flat slabs: the limelette full-scale experiments to support design model codes. FRC 2014 joint ACI-fib international workshop—fibre reinforced concrete: from design to structural applications. Montreal: Fédération internationale du béton (*fib*); 2014. p. 213–22.
27. di Prisco M, Martinelli P, Parmentier B. On the reliability of the design approach for FRC structures according to fib Model Code 2010: the case of elevated slabs. *Struct Concr*. 2016;17(4): 588–602. <https://doi.org/10.1002/suco.201500151>
28. EN 14651. Test method for metallic fibered concrete—measuring the flexural tensile strength (limit of proportionality [LOP], residual), Brussels; 2004.
29. Colombo M, Martinelli P, di Prisco M. On the evaluation of the structural redistribution factor in FRC design: a yield line approach. *Mater Struct Constr*. 2017;50(1):1–18. <https://doi.org/10.1617/s11527-016-0969-3>
30. Dassault Systèmes. Abaqus analysis user's manual—version 6.14. 2016.
31. Lubliner J, Oliver J, Oller S, Oñate E. A plastic-damage model for concrete. *Int J Solids Struct*. 1989;25(3):299–326. [https://doi.org/10.1016/0020-7683\(89\)90050-4](https://doi.org/10.1016/0020-7683(89)90050-4)
32. Lee J, Fenves GL. Plastic-damage model for cyclic loading of concrete structures. *J Eng Mech*. 1998;124(8):892–900. [https://doi.org/10.1061/\(ASCE\)0733-9399\(1998\)124:8\(892\)](https://doi.org/10.1061/(ASCE)0733-9399(1998)124:8(892))
33. Alfarah B, López-Almansa F, Oller S. New methodology for calculating damage variables evolution in plastic damage model for RC structures. *Eng Struct*. 2017;132:70–86. <https://doi.org/10.1016/j.engstruct.2016.11.022>
34. van der Aa P, van den Bos A. Material characterisation for non-linear finite element analysis (NLFEA). In: Serna P, Llano-Torre A, Martí-Vargas J, Navarro-Gregori J, editors. *Fibre reinforced concrete: improvements and innovations*. BEFIB 2020. RILEM Bookseries. Volume 30. Switzerland: Springer, Cham; 2021. https://doi.org/10.1007/978-3-030-58482-5_46
35. Roelfstra P, Wittmann F. Numerical method to link strain softening with failure of concrete. In: Wittmann F, editor. *Fracture toughness and fracture energy of concrete*. Netherlands: Elsevier Science Publishers; 1986. p. 163–75.
36. Salehian H, Barros JAO. Prediction of the load carrying capacity of elevated steel fibre reinforced concrete slabs. *Compos Struct*. 2017;170:169–91. <https://doi.org/10.1016/j.compstruct.2017.03.002>

AUTHOR BIOGRAPHIES

Giulio Zani, Assistant Professor of Structural Engineering, Department of Civil and Environmental Engineering, Politecnico di Milano, Milan, Italy.

Paolo Martinelli, Associate Professor of Structural Engineering, Department of Civil and Environmental Engineering, Politecnico di Milano, Milan, Italy.

Marco di Prisco, Full Professor of Structural Engineering, Department of Civil and Environmental Engineering, Politecnico di Milano, Milan, Italy.

How to cite this article: Zani G, Martinelli P, di Prisco M. Role of the tensile constitutive modeling on the structural response of fiber reinforced concrete flat slabs: A numerical study. Structural Concrete. 2022. <https://doi.org/10.1002/suco.202200186>